AGU PUBLICATIONS

JGR

Journal of Geophysical Research: Oceans

RESEARCH ARTICLE

10.1002/2015JC010993

Projected changes to Tasman Sea eddies in a future climate

Eric C. J. Oliver[1,2], Terence J. O'Kane[3], and Neil J. Holbrook[1,2]

[1]Institute for Marine and Antarctic Studies, University of Tasmania, Hobart, Tasmania, Australia, [2]Australian Research Council Centre of Excellence for Climate System Science, Hobart, Tasmania, Australia, [3]CSIRO Oceans and Atmosphere, Hobart, Tasmania, Australia

Key Points:
- Projected increase in the number and of warm-core eddies in the EAC Extension
- Related to changes in baroclinic and barotropic instabilities near the EAC separation point
- Leads to nearly a doubling of eddy-related southward heat transport by the 2060s

Supporting Information:
- Supporting Information S1
- Supporting Information S2

Correspondence to:
E. C. J. Oliver,
eric.oliver@utas.edu.au

Citation:
Oliver, E. C. J., T. J. O'Kane, and N. J. Holbrook (2015), Projected changes to Tasman Sea eddies in a future climate, *J. Geophys. Res. Oceans*, *120*, 7150–7165, doi:10.1002/2015JC010993.

Received 21 MAY 2015
Accepted 23 SEP 2015
Accepted article online 29 SEP 2015
Published online 6 NOV 2015

Abstract The Tasman Sea is a hot spot of ocean warming, that is linked to the increased poleward influence of the East Australian Current (EAC) over recent decades. Specifically, the EAC produces mesoscale eddies which have significant impacts on the physical, chemical, and biological properties of the Tasman Sea. To effectively consider and explain potential eddy changes in the next 50 years, we use high-resolution dynamically downscaled climate change simulations to characterize the projected future marine climate and mesoscale eddies in the Tasman Sea through the 2060s. We assess changes in the marine climate and the eddy field using bulk statistics and by detecting and tracking individual eddies. We find that the eddy kinetic energy is projected to increase along southeast Australia. In addition, we find that eddies in the projected future climate are composed of a higher proportion of anticyclonic eddies in this region and that these eddies are longer lived and more stable. This amounts to nearly a doubling of eddy-related southward temperature transport in the upper 200 m of the Tasman Sea. These changes are concurrent with increases in baroclinic and barotropic instabilities focused around the EAC separation point. This poleward transport and increase in eddy activity would be expected to also increase the frequency of sudden warming events, including ocean temperature extremes, with potential impacts on marine fisheries, aquaculture, and biodiversity off Tasmania's east coast, through direct warming or competition/predation from invasive migrating species.

1. Introduction

Subtropical western boundary currents around the world have been generating hot spots of ocean warming [*Wu et al*., 2012]. Specific to the focus of this paper, the upper ocean and surface waters of the western Tasman Sea, in the South Pacific Ocean off southeast Australia, have been warming at ~3–4 times the global average rate [*Holbrook and Bindoff*, 1997; *Ridgway*, 2007]. Significant impacts of this warming are being experienced in the marine ecology off southeastern Australia. The warming has facilitated a poleward expansion of warm-water species displacing indigenous cold-water species. In Australia, these cold-water species cannot migrate further south as they are limited by the extent of the continental shelf south of Tasmania [*Last et al*., 2010; *Johnson et al*., 2011]. To properly inform and develop adaptation strategies for these marine ecosystems [*Frusher et al*., 2014], we require accurate projections of change, and a good understanding of the underlying mechanisms, in the marine environment off southeast Australia.

The East Australian Current (EAC) is the western boundary current of the South Pacific Gyre and flows south along the east coast of Australia [*Hamon*, 1965; *Boland and Church*, 1981; *Ridgway and Dunn*, 2003] where it impacts local marine climate through the southward transport of heat and salinity from the Tropics. At approximately 33°S, the EAC partially separates from the coast [*Godfrey et al*., 1980], delineating the quasi-steady flow to the north from the highly variable EAC Extension to the south (see schematic representation of circulation in Figure 1a). The EAC Extension is an unsteady flow consisting of a train of mesoscale eddies, many of which are generated from the separation of the EAC from the coast, which propagate southward as far as Tasmania [*Nilsson and Cresswell*, 1980; *Everett et al*., 2012; *van Sebille et al*., 2012]. These eddies can trap fluid parcels and thereby transport water properties southward with them, including warm or cold-water anomalies, nutrients, and even marine larvae [*Suthers et al*., 2011; *Everett et al*., 2012; *van Sebille et al*., 2012]. In doing so, these eddies have a significant impact on the physical, chemical, and biological properties of the ocean off southeast Australia. Understanding how these eddies and their properties are projected

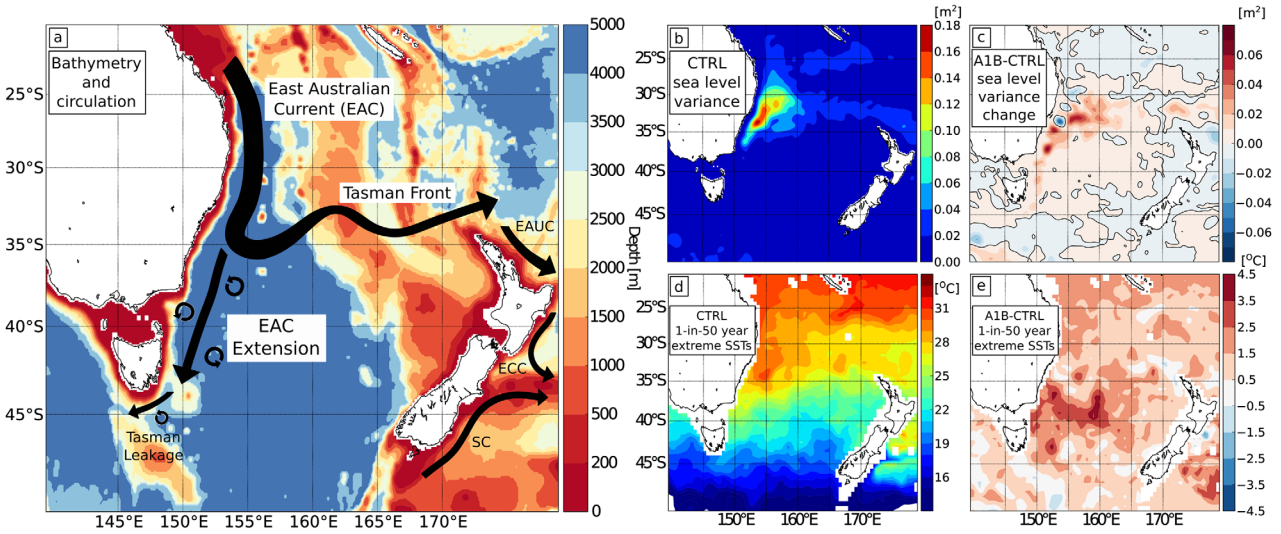

Figure 1. Circulation off southeast Australia and projected changes to eddy variability and temperature extremes. (a) Bathymetry in the Tasman Sea and a schematic representation of the East Australian Current (EAC), Tasman Front, and EAC Extension circulation system. The currents to the north and east of New Zealand are the East Auckland Current (EAUC), the East Cape Current (ECC), and the Southland Current (SC). (b) Sea level variance, a proxy for eddy kinetic energy, for the 1990s decade from the CTRL simulation and (c) its projected change by the 2060s from the A1B simulation. (d) One-in-50-year return level of sea surface temperature extremes for the 1990s decade from the CTRL simulation and (e) its projected change by the 2060s from the A1B simulation. Figures are adapted from *Oliver et al.* [2014] and *Oliver and Holbrook* [2014].

to change under anthropogenic climate change is critical for projecting changes to the marine climate, fisheries, and biodiversity off southeast Australia.

The transport associated with the EAC and EAC Extension circulation has undergone significant changes in recent years and is projected to also further change significantly under anthropogenic climate change. The "spin-up" of the South Pacific Gyre has been linked to increases in the sea surface height in the interior of the gyre (by 12 cm between 1993 and 2004) and an increase of wind stress curl over the South Pacific [*Roemmich et al.*, 2007]. Multidecadal changes in ocean climate off southeast Australia (represented by temperature and salinity measured at Maria Island since 1945) have been found to be due to an increased southward influence of the EAC [*Ridgway*, 2007]. It has been suggested that these observed changes in ocean climate are also linked to the basin wide changes in wind stress curl over the South Pacific [*Hill et al.*, 2008]. Furthermore, *Cetina-Heredia et al.* [2014] found a significant increase in southward transport across the EAC separation point and that this could be attributed to increased transport within eddies. *Sloyan and O'Kane* [2015] showed that since 1948 there has been a significant increase in EAC Extension transport and a decrease in Tasman Front and EAC transports where the anomalously weaker EAC transport at 25°S is associated with large-scale changes in the Tasman Sea, specifically stronger stratification above the thermocline, larger thermocline temperature gradients, and enhanced energy conversion.

Dynamically downscaled global climate change projections indicate that by the year 2060, under an A1B carbon emission scenario, the southward transport in the EAC Extension is projected to increase by ~4 Sv corresponding also to a reduced eastward transport along the Tasman Front [*Oliver and Holbrook*, 2014]. *Oliver and Holbrook* [2014] demonstrated that these projected changes in transport are consistent with the linear barotropic response of the ocean to increased wind stress curl, primarily over latitudes south of the EAC separation point. In addition to the change in transport, *Matear et al.* [2013] and *Oliver and Holbrook* [2014] showed that the energy associated with eddy activity in the Tasman Sea is projected to increase, particularly along the EAC Extension (Figures 1b and 1c), and that this is associated with an increased nutrient supply and primary productivity in the upper ocean [*Matear et al.*, 2013]. Furthermore, *Oliver et al.* [2014] showed that projected changes in sea surface temperature (SST) extremes are not colocated with the mean warming hot spot in the Tasman Sea (Figures 1d and 1e) but rather related to increases in both the mean SST (overall warming) and SST variability (due to greater eddy activity).

In this paper, we show that there is a change in the eddy field projected for the 2060s compared with representative eddy characteristics in the 1990s. The projected change in characteristics includes a significant increase in the presence of anticyclonic eddies, relative to cyclonic eddies, including a greater propensity of

eddies that are more stable and longer lived. These changes in the overall composition and characterization of the Tasman Sea eddy field are concurrent with upper ocean warming, changes in vertical stratification, and increased potential energy in the thermocline. We demonstrate that these changes are consistent with theoretical understanding of eddy formation in response to projected increases in energy transfer rates due to baroclinic and barotropic instabilities.

2. Data and Methods

We have used dynamical downscaled ocean model simulations for the 1990s and 2060s decades (section 2.1) and calculated statistics of tracked mesoscale eddies (section 2.2), heat and freshwater advection (section 2.3), and measures of barotropic and baroclinic instability (section 2.4).

2.1. Eddy-Resolving Ocean Model Simulations

Dynamically downscaled ocean model simulations for the 1990s and 2060s decades were used to investigate the response of ocean circulation and eddies in the Tasman Sea to climate change. The Ocean Forecasting Australia Model (OFAM) [*Oke et al.*, 2008] was used to perform the downscaling using forcing derived from a historical atmospheric reanalysis (details below) to represent the present-day climate. A climate change projected simulation using the CSIRO Mk3.5 climate model (under an A1B emissions scenario) was used to represent the projected future forcing [*Chamberlain et al.*, 2012; *Sun et al.*, 2012]. The OFAM model domain is quasi-global (70°S and 70°N) with 1/10° horizontal resolution (eddy resolving) around Australia (90°E–180°E, 70°S–20°N); the horizontal resolution coarsens as we move away from Australia, up to 2° in the North Atlantic Ocean. The model consists of 47 z levels with 10 m vertical resolution in the upper 200 m.

We analyze two separate decades of ocean simulations representing regionally downscaled global climates in this study: the control simulation (CTRL) representing the 1990s and a future projected simulation (A1B) representing the 2060s under the A1B carbon emissions scenario. OFAM was forced repeatedly by "normal-year" prescribed fluxes in both simulations. For the CTRL simulation, this consists of ocean surface fluxes of heat, freshwater, and momentum derived from the European Centre for Medium-Range Weather Forecasts (ECMWF) Reanalysis output (ERA-40) [*Uppala et al.*, 2005] with variability on time scales longer than 1 year filtered out and with large-scale climate modes (e.g., El Ninõ-Southern Oscillation, Indian Ocean Dipole) in their neutral states (for further details see *Chamberlain et al.* [2012]). The prescribed fluxes for the A1B simulation were calculated by taking the prescribed fluxes applied to the CTRL simulation and adding to them the projected change between the 1990s and 2060s decades derived from CSIRO Mk3.5 global climate model simulations under an A1B emissions scenario. For both simulations, we obtained three-dimensional fields of sea surface height $\eta(x,y,z,t)$ (m), horizontal currents $u(x,y,z,t)$ and $v(x,y,z,t)$ (m s^{-1}), temperature $T(x,y,z,t)$ (°C), and salinity $S(x,y,z,t)$ (PSU). Here (x, y, z) are the zonal, meridional, and vertical spatial dimensions, respectively, and t is the time dimension. Both simulations have a 16 year spin-up period, and we analyzed the last 9 years of simulation output. The time step of the model output fields is daily for the surface, eight-daily for the upper 200 m, and monthly for the full depth data.

We decomposed each state variable into a sum of the climatological seasonal cycle, denoted by a subscript S, and perturbations from this, denoted by a prime, e.g., for zonal velocity:

$$u(x,y,z,t)=u_S(x,y,z,t)+u'(x,y,z,t) \quad (1)$$

The climatological seasonal cycle is the sum of the time mean and an estimate of seasonal variations calculated by harmonic regression onto the annual and semiannual cycles. The perturbations are also referred to as the transient component; we do not refer to this as the eddy component as we reserve this term specifically for mesoscale eddies (see section 2.3 for further discussions).

2.2. Eddy Detection and Tracking

Mesoscale eddies in the CTRL and A1B simulations were detected and tracked using daily fields of sea surface height and the recently developed algorithm of *Chelton et al.* [2011a] (details of our implementation are provided in Appendix A). We have calculated a suite of summary statistics from the detected and tracked eddies for the CTRL and A1B simulations. These statistics are evaluated within 1°×1° bins and include (i) the total number of eddies per bin, (ii) the average eddy amplitude in each bin, and (iii) the proportion of cyclonic and anticyclonic eddies in each bin. The properties of a composite EAC Extension eddy

were also calculated by averaging the fields of η, T, S, u, and v centered on all eddy centroids within the EAC Extension region. This region was defined as south of 33°S, north of 47°S, east of the continental landmass, and west of a straight line running from (33°S, 157.5°E) to (47°S, 150°E). The properties of the composite eddy are defined in cylindrical coordinates, e.g., $T_{\text{eddy}}(r, z, \theta)$, where r is the radius from the eddy center, z is depth, and θ is angle.

2.3. Temperature Transport

The time-averaged meridional temperature transport (J s^{-1}) through a zonal (latitudinal) section is given by [e.g., *Peixoto and Oort*, 1992]

$$\phi = \int_{-h}^{0} \int_{x_1}^{x_2} \rho_0 c_0 \overline{vT}\, dxdz \tag{2}$$

where $[-h, 0]$ and $[x_1, x_2]$ are the ranges of integration in the vertical and zonal directions over the latitudinal section, respectively, ρ_0 is the density of seawater (approximated by the constant 1024 kg m^{-3}), c_0 is the specific heat of seawater (4187 J kg^{-1} °C^{-1}), an overbar represents the time mean, and $\overline{vT}$ is the Reynolds averaged meridional advection (v) of temperature (T). Note that the terminology of "temperature transport" is more appropriate than "heat transport" when mass is not conserved over an area of integration [e.g., *Talley*, 2003]. In the present study, our analysis approach does not attempt to conserve mass. Hence, we follow the language used in previous studies and identify our estimated transports in units of WT (J s^{-1}) instead of W (J s^{-1}) to articulate this point of difference. The decomposition of velocity and temperature into seasonal and transient components (equation (1)) leads to the following four temperature transport terms:

$$\phi = \underbrace{\rho_0 c_0 < \overline{v_S T_S} >}_{\phi_{SA}} + \underbrace{\rho_0 c_0 < \overline{v_S T'} > + \rho_0 c_0 < \overline{v' T_S} >}_{\phi_{STA}} + \underbrace{\rho_0 c_0 < \overline{v' T'} >}_{\phi_{TA}} \tag{3}$$

where $< \cdot > = \int_{-h}^{0} \int_{x_1}^{x_2} \cdot dxdz$ represents the double integral over the latitudinal section. We define the climatological seasonal temperature transport ϕ_{SA} as the first term (the "seasonal advective" component), the transient-related temperature transport ϕ_{TA} as the fourth term (the "transient advective" component), and the coupled seasonal-transient temperature transport ϕ_{STA} as the sum of the second and third terms. The subscript A refers to the "advection" of temperature, as opposed to the heat transported by eddies (more details below). Temperature transports were calculated along the western boundary of the Tasman Sea by integrating vertically over 0–200 m and zonally over a band of 10° longitude bounded on the west by the shelf break (or 147°E south of Tasmania). Time-mean values were calculated over the eight-daily model output which extends down to 200 m depth; data below 200 m were only available on a monthly time scale which is too long to effectively resolve the variability associated with mesoscale eddies.

We are also interested in the temperature transported by mesoscale eddies which is not easily extracted from the seasonal plus transient decomposition above (equation (3)). The transient advective component ϕ_{TA} is often referred to as the "eddy" component. However, the temperature transport associated with mesoscale eddies can also be expressed within the seasonal advective component ϕ_{SA}. For example, consider a train of warm-core anticyclonic eddies traveling southward along the EAC Extension. Since each eddy follows a similar path, there will also implicitly be a time-averaged expression of the eddy-related meridional velocity in $\overline{v_S}$ (i.e., southward nearer to the coast and northward further offshore) and so also in ϕ_{SA}. Therefore, we cannot take ϕ_{TA} alone as being uniquely representative of the total temperature transport by mesoscale eddies.

We develop here an alternative approach to estimate the temperature transported by mesoscale eddies based on summing the heat content of each eddy as it crosses a latitudinal section. The heat content of the ith mesoscale eddy $q_{E,i}$ (J) is given by integrating the heat content over the cylindrical volume of the eddy [e.g., *Joyce et al.*, 1981]:

$$q_{E,i} = \int_0^R \int_{-h}^{0} \int_0^{2\pi} \rho_0 c_0 T_{\text{eddy},i}(r, z, \theta) r d\theta dz dr \tag{4}$$

where R is the outer radius enclosing the heat contained within the eddy and $T_{\text{eddy},i}$ is the temperature structure of the ith eddy expressed in cylindrical coordinates. The value of R does not vary significantly with

depth over the upper 200 m (based on depth profiles of composite eddies, supporting information Figure S1). We use the eddy scale determined by the eddy tracking algorithm as our radius R: *Early et al.* [2011] demonstrate a high retention of tracer trapped within the zero contour of relative vorticity, which can be approximated by this eddy scale [*Chelton et al.*, 2011a]. Note that the heat content of an eddy can be broken up into the sum of component contributions from seasonal temperatures ($T_{S,eddy}$) and transient temperatures (T'_{eddy}):

$$q_{E,i} = \underbrace{\rho_0 c_0 [T_{S,eddy,i}]}_{q_{SE,i}} + \underbrace{\rho_0 c_0 [T'_{eddy,i}]}_{q_{TE,i}} \tag{5}$$

where $[\cdot] = \int_0^R \int_{-h}^0 \int_0^{2\pi} \cdot r d\theta dz dr$ denotes the volume integral over the cylindrical eddy, $q_{SE,i}$ is the seasonal heat content of the eddy, and $q_{TE,i}$ is the transient heat content of the eddy.

The meridional heat flux, across a latitudinal section defined as above, due to mesoscale eddies is now given by time averaging the heat contribution from all eddies that cross the section northward minus the heat contribution from all eddies that cross southward

$$\phi_E = \frac{1}{\tau}\left(\sum_{i=1}^{N_N} q_{E,i} - \sum_{i=1}^{N_S} q_{E,i}\right) \tag{6}$$

where N_N and N_S are the number of northward and southward propagating eddies, respectively, and τ is the total time over which these crossings occurred (i.e., 9 years of model simulation). The decomposition of eddy heat content into seasonal and transient components can be carried through the meridional heat flux definition to give

$$\phi_E = \underbrace{\frac{1}{\tau}\left(\sum_{i=1}^{N_N} q_{SE,i} - \sum_{i=1}^{N_S} q_{SE,i}\right)}_{\phi_{SE}} + \underbrace{\frac{1}{\tau}\left(\sum_{i=1}^{N_N} q_{TE,i} - \sum_{i=1}^{N_S} q_{TE,i}\right)}_{\phi_{TE}} \tag{7}$$

where ϕ_{SE} and ϕ_{TE} are the meridional heat flux due to the seasonal and transient components of the eddies, respectively.

2.4. Barotropic and Baroclinic Instability

We have calculated a set of measures related to eddy variability and instabilities from the model simulated fields of velocities, temperature, and salinity. The kinetic energy associated with the perturbation velocities, of which mesoscale eddies are a major contributor, is known as the eddy kinetic energy (EKE, in J), and the time-mean EKE within a volume V is given by

$$EKE = \frac{1}{2}\int_V \rho\left(\overline{u'^2} + \overline{v'^2}\right) dV \tag{8}$$

where $\rho(x, y, z)$ is the water density. Density was calculated from temperature and salinity using the Thermodynamic Equation of Seawater 2010 (TEOS-10) [*IOC et al.*, 2010].

Mean potential energy and mean kinetic energy are transferred to EKE by baroclinic and barotropic instabilities, respectively. The transfer rate of mean potential energy to EKE (J s^{-1}), representing baroclinic instability, is given by

$$\gamma_{PE} = g\int_V \frac{\left(\overline{u'\rho'}\frac{\partial\bar{\rho}}{\partial x} + \overline{v'\rho'}\frac{\partial\bar{\rho}}{\partial y}\right)}{\partial\tilde{\rho}/\partial z} dV \tag{9}$$

and the transfer rate of mean kinetic energy to EKE (J s^{-1}), representing barotropic instability, is given by

$$\gamma_{KE} = -\tilde{\rho}\int_V \left(\overline{u'u'}\frac{\partial\bar{u}}{\partial x} + \overline{u'v'}\left(\frac{\partial\bar{u}}{\partial y} + \frac{\partial\bar{v}}{\partial x}\right) + \overline{v'v'}\frac{\partial\bar{v}}{\partial y}\right) dV \tag{10}$$

where g is the acceleration due to gravity and $\tilde{\rho}(z)$ is a reference state for the ocean, which is approximated by the zonally and meridionally averaged density [*Böning and Budich*, 1992; *Eden and Böning*, 2002; *Mata et al.*, 2006].

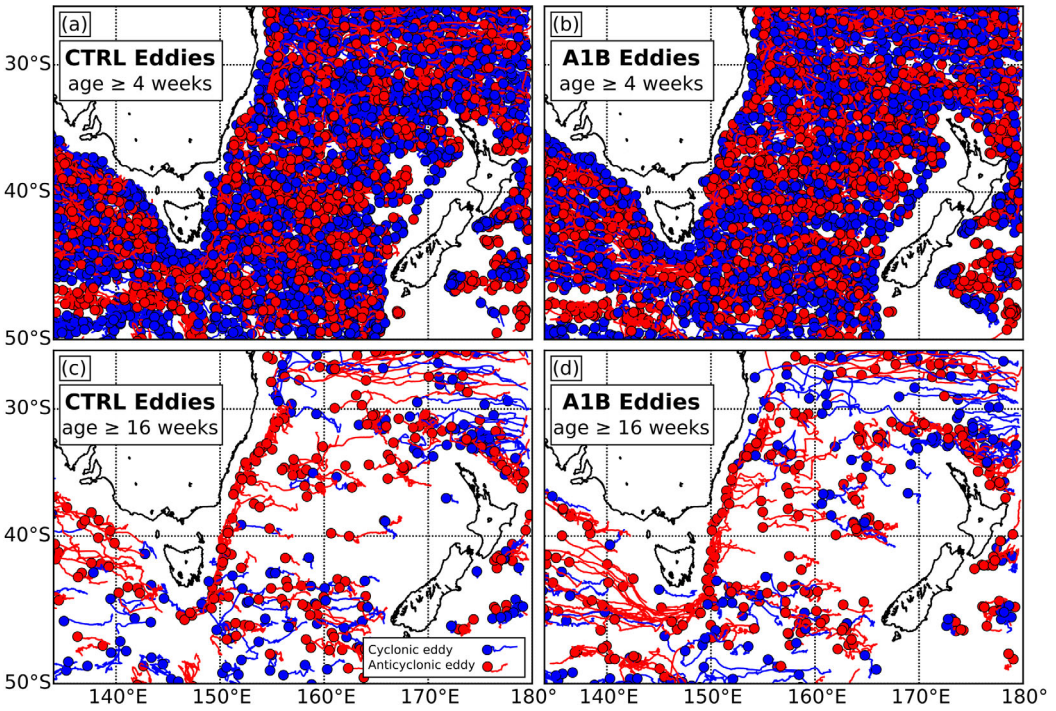

Figure 2. Tracked mesoscale eddies off of Eastern Australia. Lines indicate eddy tracks and circles indicate the end point of tracked anticyclonic (red) and cyclonic (blue) eddies in the (a, c) CTRL and (b, d) A1B simulations. Tracks are shown for all eddies with life times of at least (a, b) 4 weeks and (c, d) 16 weeks.

3. Simulated 1990s and Projected 2060s Eddy Fields

Eddy tracks in the Tasman Sea from the model simulations indicate it to be an eddy-rich region (Figure 2). For the CTRL run, the distribution of eddies with lifetimes of at least 4 weeks shows almost the entire Tasman Sea to be filled with eddies (Figure 2a). One exception is near New Zealand, presumably reflecting the nature of eddies to propagate westward and away from eastern boundaries and the broad region of relatively shallow bathymetry around New Zealand (e.g., Figure 1a). For longer-lived eddies, with lifetimes of at least 16 weeks (which are common in this region [e.g., *Chelton et al*., 2011a]), the eddy field is less homogeneous in overall spatial distribution and composition (Figure 2c). Longer-lived eddies tend to be concentrated in the western and southern Tasman Sea. Anticyclonic eddies tend to be found near the western boundary, propagating southward along the EAC Extension. Many of these eddies are generated in the EAC separation (near ~33°S) and a few manage to remain stable all along the coast of southeast Australia and around the southern tip of Tasmania to propagate into the Great Australian Bight. Cyclonic eddies tend to be found in the interior of the southern Tasman Sea and away from the coastal boundaries, although a few do propagate far enough westward to enter the EAC Extension region.

The future projected ocean state shows a change in the distribution of longer-lived eddies (compare Figures 2c and 2d). In the A1B simulation, the separation between anticylonic eddies along the western boundary and cyclonic eddies in the interior of the Tasman Sea is enhanced almost to the point of complete partition (compare Figures 2c and 2d). In addition, the anticyclonic eddies in the EAC Extension appear longer lived, with more surviving the passage around Tasmania into the Great Australian Bight. In contrast, there is no obvious difference between the CTRL and A1B run for eddies with lifetimes of at least 4 weeks (compare Figures 2a and 2b), however, this may be because too many are eddies visually saturating the plot.

Summary statistics derived from the tracked eddies (with life times of at least 8 weeks; Figure 3) act to quantify and extend the featured information in the eddy track maps. The total number of eddies tends to be highest in the western and southern Tasman Sea in both the CTRL and A1B runs (Figures 3a and 3b). The difference in total number of eddies between the two decadal periods (1990s versus 2060s) indicates a

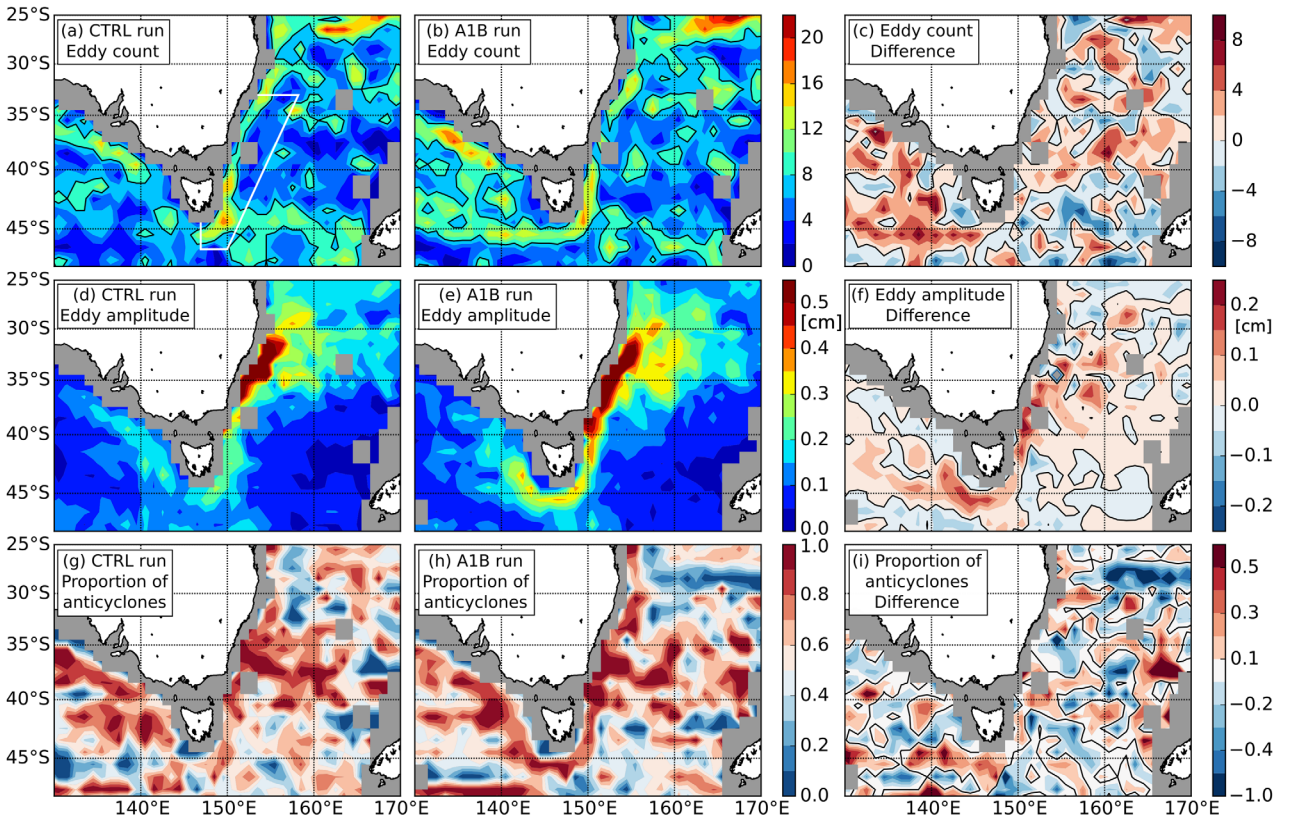

Figure 3. Summary statistics for tracked eddies with lifetimes of at least 8 weeks. (top row) Total eddy count, (middle row) average eddy amplitude, and (bottom row) proportion of anticyclonic eddies are shown for (left column) the CTRL run, (middle column) the A1B run, and (right column) their difference in 1° gridded domain. A proportion of anticyclonic eddies equal to 1 indicates 100% anticyclonic eddies in that cell, 0 indicates no anticyclonic eddies (100% cyclonic eddies), and 0.5 indicates a 50%–50% split between anticyclonic and cyclonic eddies. Grey indicates areas of no data.

slight increase of ~five eddies along the EAC Extension region projected in the next 50 years (Figure 3c). The average eddy amplitude is largest (>50 cm) near the EAC separation point and moderately large (20–50 cm) along the EAC Extension, Tasman Leakage, and Tasman Front in both runs (Figures 3d and 3e) with a projected increase of 10–20 cm in amplitude along the EAC Extension and Tasman Leakage in the A1B run (Figure 3f). Finally, there is a general preference for anticyclonic eddies along the EAC Extension and Tasman Leakage regions in the CTRL run (Figure 3g), but this is increased in the A1B run (Figures 3g and 3h) with relative proportions of anticyclonic eddies increasing in some parts from 20% to over 70% (Figure 3i).

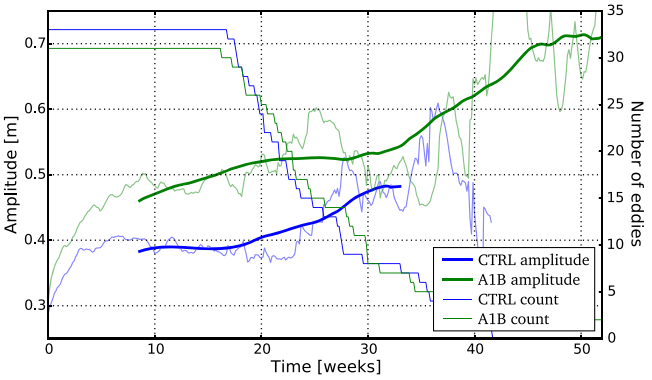

Figure 4. Amplitude of EAC Extension eddies as a function of time since generation. The thick lines show the average amplitude across all eddies that spent at least half their lifetime within the EAC Extension as a function of time since the initial eddy detection ("generation") for the CTRL run (blue) and the A1B run (green). The thickest lines show a 121 day moving average of the time series. The thin lines show the total number of eddies that contribute to each average.

We found that the future projected ocean exhibited larger amplitude, longer-lived eddies in the EAC Extension region (Figure 4). For this purpose, the EAC Extension region is defined as south of 33°S, north of 47°S, east of the continental landmass, and west of a straight line running from (33°S, 157.5°E) to (47°S, 150°E; this region is indicated in Figure 3a, white outline). For all eddies

Table 1. Properties of Composite EAC Extension Eddies in the CTRL and A1B Simulations[a]

	Anticyclonic		Cyclonic	
	CTRL	A1B	CTRL	A1B
Count	1628	1525	3248	3635
Count (≥8 weeks)	96	95	42	45
Amplitude (cm)	25.9	31.6	8.1	8.4
Scale (km)	92.8	95.6	78.2	77.6
Average age (days)	13.9	15.3	7.0	6.1
Mean T (°C)	18.1	19.8	17.5	19.1
Mean T anomaly (°C)	0.55	0.60	−0.58	−0.62
Heat content (10^{20} J)	4.01	4.88	3.33	3.77
Heat content anomaly (10^{20} J)	0.142	0.169	−0.133	−0.144

[a]Count indicates the number of eddies that contributed to the average; Count (≥8 weeks) indicates the subset of those eddies that lasted at least 8 weeks.

that spent at least half their lifetime within this region, the average amplitude, across all eddies, was calculated as a function of time since eddy generation. Eddies in the CTRL run have a growth period of about 5 weeks over which the amplitude increases from 30 to 40 cm and then weakly increases up to 50 cm over weeks 10 through 30. Eddies in the A1B grow to about 50 cm in the first 10 weeks and continue to grow, reaching up to 70 cm after 52 weeks (1 year). It should be noted that mesoscale eddies in the model simulations are biased to longer lifetimes, as compared with the observed record [i.e., *Chelton et al*., 2011a]. Nonetheless, the sign and magnitude of change between the CTRL and A1B runs is remarkable.

4. Composite Eddies and Meridional Temperature Transport

We found a clear signal of change in the morphology of the composite anticyclonic eddies in the EAC Extension between the CTRL and A1B runs, including changes in the horizontal scale, amplitude (vertical scale), shape, structure, and angular velocity (Table 1 and Figure 5). Anticyclonic eddies in the CTRL run had a peak η'_{eddy} of around 18 cm while in the A1B run they had a peak η'_{eddy} of around 26 cm, a change that is also expressed in the increased angular velocity of these eddies (Figures 5a–5c). Anticyclonic eddies in the CTRL run had a mean T'_{eddy} of 0.55°C while in the A1B run they had a mean T'_{eddy} of 0.60°C (Table 1) which was superimposed on an overall change in ambient $T_{S,eddy}$ of 1.7°C in the EAC Extension (Table 1). The change in T'_{eddy} was not distributed uniformly across the eddy: the southwestern corner of the eddy experienced the greatest warming (depth-averaged temperature; Figure 5f). This temperature increase was expressed as a change in the total heat content q_E from 4.01×10^{20} to 4.88×10^{20} J (∼22% increase); the increase in T'_{eddy} alone led to an increase in heat content anomaly q_{TE} from 0.142×10^{20} to 0.169×10^{20} J (∼19% increase; Table 1). These heat content values for the upper-ocean (0–200 m) portion of the eddy are generally consistent with the estimates of *Morrow et al*. [2003] for Leeuwin Current eddies.

Composite cyclonic eddies in the EAC Extension did not show a clear signal of change between the CTRL and A1B runs (Table 1 and Figure 5). Peak η'_{eddy} was enhanced slightly, O (1 cm), and was not accompanied by a coherent change in angular velocity (Figures 5g–5i). Similarly, there was very little projected change in mean T'_{eddy} (Figure 5j–5l) and correspondingly very little change in heat content anomaly (-0.133×10^{20} to -0.144×10^{20} J; Table 1). Therefore, the projected change in total heat content of cyclonic eddies, from 3.33×10^{20} to 3.77×10^{20} J, was dominated by the 1.6°C increase in ambient $T_{S,eddy}$. In addition, cyclonic eddies were much shorter lived (on average: 8.1 days in CTRL, 8.4 days in A1B) than anticyclonic eddies (25.9 days in CTRL, 31.6 days in A1B; Table 1).

It should be noted that the change in composite mean eddy between the CTRL and A1B runs is within the standard deviation of all eddies from either run. Therefore, the projected future mean composite eddy lies within the probability distribution of EAC eddies from the CTRL run. However, we found that larger changes occurred in the extreme eddies, particularly in the extreme anticyclonic eddies. The upper decile of anticyclonic eddies had mean properties that exhibited projected changes much greater than the projected changes for the mean composite eddies. Eddy amplitudes increased from 61.3 to 71.6 cm and eddy scales increased from 130.7 to 136.0 km. Eddy heat content anomaly increased from 4.36×10^{19} to 5.18×10^{19} J, a much larger increase than for the mean composite eddy. Cyclonic eddies showed a weaker increase in the mean properties of the upper decile, with amplitudes and scales actually decreasing from 16.2 to 15.8 cm and from 117.6 to 117.4 km, respectively. Heat content anomaly changed from -3.92×10^{19} to -4.10×10^{19} J, a weaker change than the corresponding change in anticyclonic heat content Mesoscale eddies contributed significantly to both seasonal

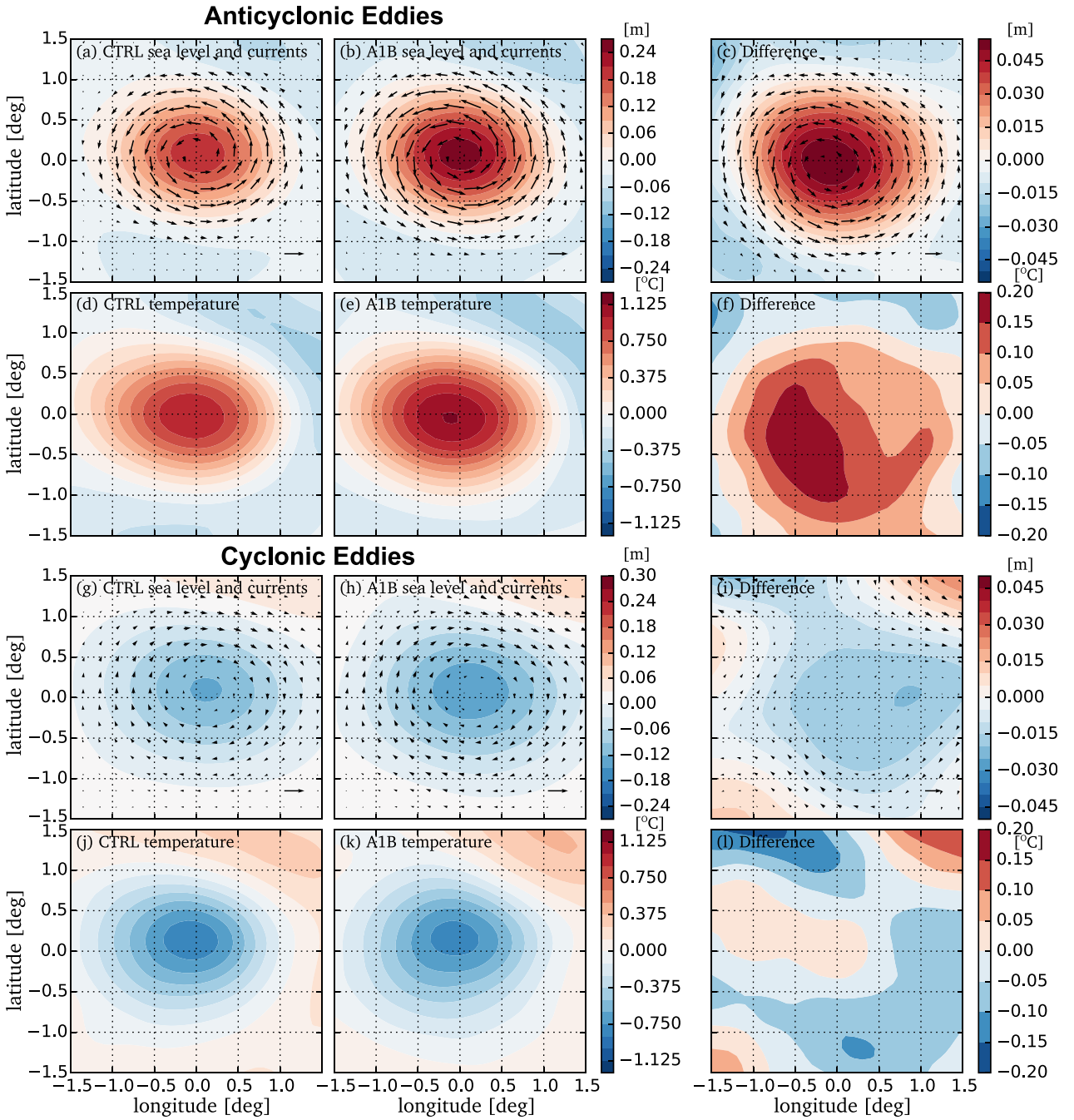

Figure 5. Composite EAC Extension eddies. Shown are the sea level and (a–c, g–i) depth-averaged current anomalies and (d–f, j–l) depth-averaged temperature anomalies for composite anticyclonic (top six plots) and cyclonic (bottom six plots) eddies in the EAC Extension for (left column) the CTRL run, (middle column) the A1B run, and (right column) their difference. The reference arrows in Figures 5d, 5f, 5g, and 5h and Figures 5c and 5i represent 0.4 and 0.1 m s^{-1}, respectively.

and transient meridional temperature transport in the EAC Extension (Figure 6). In the CTRL run, the seasonal advective heat flux ϕ_{SA} was negative (southward) over the entire EAC system reducing from −0.9 PWT at 32°S (consistent with shallow EAC estimates from *Talley* [2003]) to −0.1 PWT at 36°S, −0.03 PWT at 42°S, and dropping to zero at 44°S (Figure 6a, solid black line). The seasonal eddy heat flux ϕ_{SE} was also negative over the EAC Extension and relatively constant over 36°S–44°S, between −0.01 and −0.03 PWT, becoming dominant over ϕ_{SA} south of 39°S (Figure 6a, dashed black line). This implies that south of 39°S, meridional temperature transport was dominated by transport within mesoscale eddies,. while north of 39°S, meridional temperature transport is dominated by other processes (i.e., processes other than coherent mesoscale eddies, such as steady

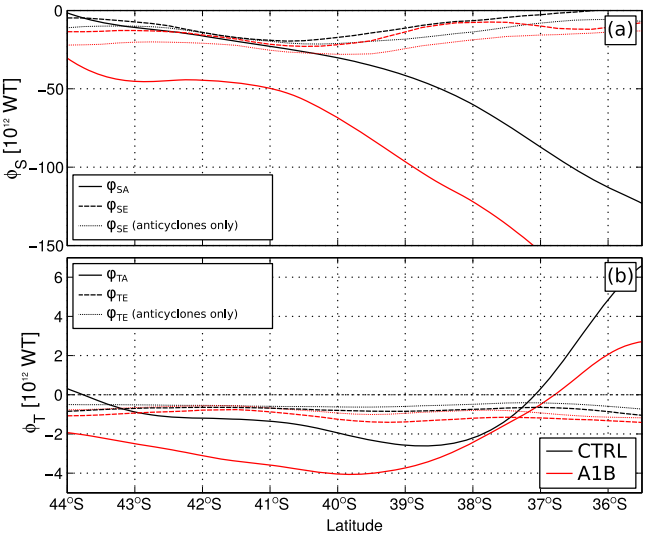

Figure 6. Meridional temperature transport off southeast Australia. Shown are (a) the seasonal temperature transport (ϕ_S) and (b) the transient temperature transport (ϕ_T) for the CTRL run (black line) and the A1B run (red line) derived by Reynolds averaging *vT* (the "advective" component; solid lines) and by averaging the contribution due to mesoscale eddies (the "eddy-related" component; dashed and dotted lines). These quantities are shown as a function of latitude, integrated vertically over 0–200 m and zonally over a band of 10° longitude bounded on the west by the shelf break (or 147°E south of Tasmania). Note the large difference in vertical scales between the two plots.

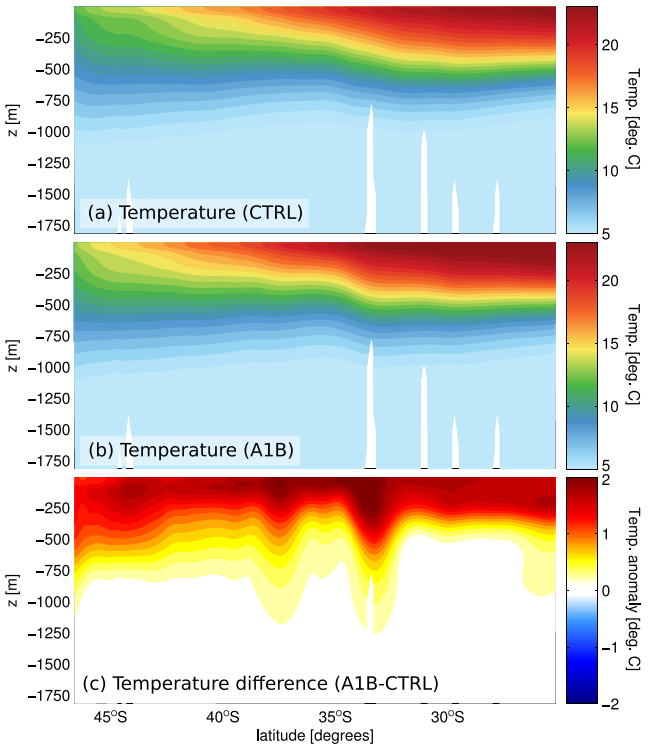

Figure 7. Projected warming in the upper ocean off southeast Australia. The average ocean temperature is shown as a function of depth and latitude (averaged zonally over a band of 10° longitude bounded on the west by the shelf break or 147°E south of Tasmania) for (a) the CTRL run, (b) the A1B run, and (c) their difference.

mean flow or unsteady flows including filaments or small eddies undetected by the eddy algorithm). In the A1B run, ϕ_{SA} was also southward over the entire EAC Extension and increased relative to the CTRL run by 0.03 PWT in the south (44°S) to 0.18 PWT in the north (36°S; Figure 6a, solid red line). As with the CTRL, ϕ_{SE} in the A1B run was negative over the EAC Extension and increased along with ϕ_{SA} becoming dominant south of 39°S (Figure 6a, dashed red line). In addition, over much of the EAC Extension (i.e., south of 39°S), the ϕ_{SE} in the A1B run increased over that in the CTRL run by up to a factor of 2 at more southern latitudes (Figure 6a, compare black and red dashed lines), and anticyclonic eddies alone were responsible for substantially more of this temperature transport (Figure 6a, compare thick and thin dashed lines).

The transient temperature transport ϕ_T in the EAC Extension was much weaker, by 1 order of magnitude, than the seasonal temperature transport (Figure 6b). However, as with ϕ_S, the advective component ϕ_{TA} was southward over most of the EAC Extension (south of 37°S) and increased substantially in the A1B run. The eddy-related component ϕ_{TE} was also southward over the entire domain and increased between the CTRL and A1B run everywhere. As with the seasonal component, the eddy-related component made up a significant portion of the total temperature transport particularly at the more southerly latitudes.

5. Mechanism: Climate Change Influences on Mesoscale Instabilities

Concurrent with the projected changes in the eddy field is a significant warming of the upper ocean off southeast Australia (Figure 7). The time-mean temperature averaged over a zonal band of 10° longitude bounded on the west by the shelf break or 147°E south of Tasmania shows a similar overall meridional structure in both the CTRL and A1B runs (Figures 7a and 7b). Note

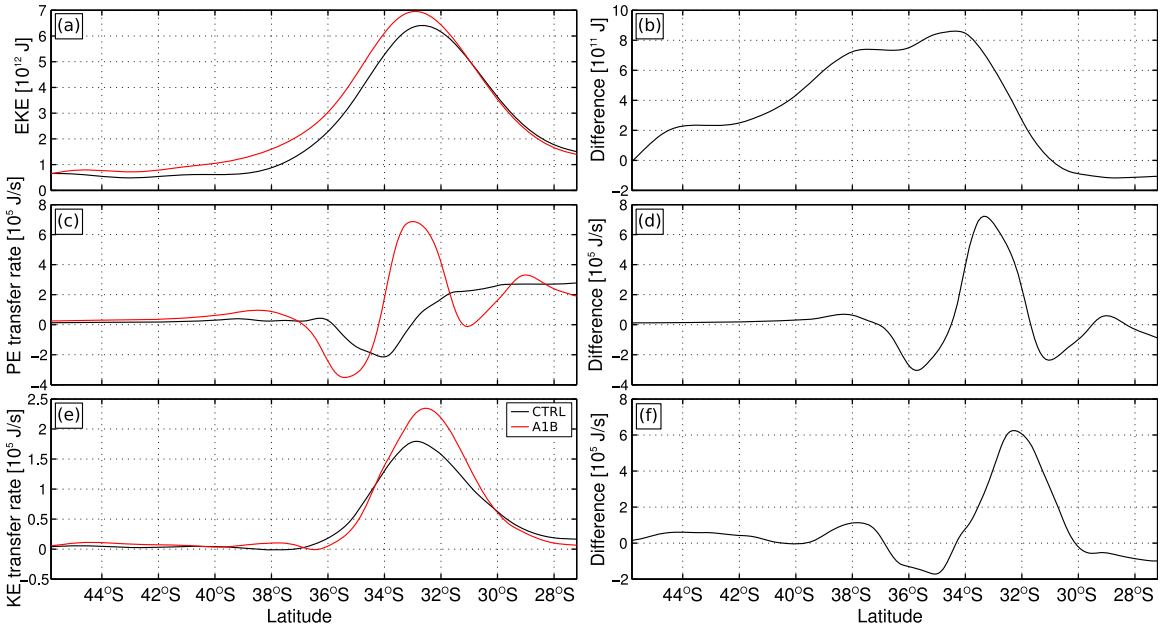

Figure 8. (top) Eddy kinetic energy (EKE) and rates of energy conversion to EKE from (middle) mean potential energy (γ_{PE}, due to baroclinic instability) and (bottom) mean kinetic energy (γ_{KE}, due to barotropic instability) for (left) the CTRL run (black line) and the A1B run (red line) and (right) their difference. These quantities are shown as a function of latitude, integrated vertically over 0–1500 m (which is sufficient to capture the depth range of instability [e.g., *O'Kane et al.* [2011]) and zonally over a band of 10° longitude bounded on the west by the shelf break (or 147°E south of Tasmania).

that this is not the same region used before (see Figure 3a) but is very similar, largely overlapping, and more convenient for the calculation of instabilities. The pattern of change in temperature between the two runs shows a warming of 1–2°C focused in the upper 500 m across all latitudes (Figure 7c). The thermocline depth, defined by a maximum in dT/dz, has not changed between the two runs along southeastern Australia (not shown). However, the increased stratification has likely increased lateral density differences and available potential energy in the separation region. More energy in the thermocline in the EAC separation region would lead to larger anomalies (i.e., eddies) associated with eddy generation.

This increased upper-ocean energy is reflected in changes to the mean EKE and baroclinic and barotropic instabilities along the EAC Extension (Figure 8). The mean EKE, which tends to peak near the EAC separation point (~33°S), is projected to increase from around the EAC separation point southward all along the EAC Extension to ~45°S (Figures 8a and 8b). The transfer rate of energy from mean potential energy to EKE, γ_{PE}, representing baroclinic instabilities associated with the growth of eddies, is high north of the separation point in the CTRL and is projected to increase significantly at the separation point in the A1B run (Figures 8c and 8d). The transfer rate of energy from mean kinetic energy to EKE, γ_{KE}, representing barotropic instabilities associated with the long-term stability of eddies, is high in the region of large EKE and is smaller than γ_{PE} by a factor of ~4. The projected change in γ_{KE} in the A1B run has a very similar pattern to the projected change in γ_{PE}, i.e., large increases localized around the EAC separation point with weaker changes elsewhere (Figures 8e and 8f). These results are also consistent with the study of *Sloyan and O'Kane* [2015] who showed systematic changes associated with warmer SSTs in the Tasman Sea over the recent decades has resulted in stronger stratification above the thermocline, larger thermocline temperature gradients, and enhanced transfer rates of mean to transient potential energy (i.e., increased baroclinic instability conversion).

6. Discussion and Conclusions

This study has investigated projected future changes to the mesoscale eddy field along the southeast coast of Australia from eddy-resolving ocean model simulations based on dynamically downscaled global climate change projections. The model simulations consisted of a historical run, with reanalysis-derived surface forcing representative of the 1990s, and a projected run, with projected changes in surface forcing to the 2060s

derived from a global climate model under the A1B anthropogenic carbon emissions scenario. Mesoscale eddies were identified and tracked using sea level anomalies and a set of eddy statistics were calculated from these eddy tracks. We found that there is a projected increase in the number of anticyclonic eddies, relative to cyclonic eddies, south of the EAC separation point. In addition, we found that these anticyclonic eddies are more stable and longer lived than for the present-day climate. This increase in anticyclonic eddies generates nearly a doubling of eddy-related southward temperature transport in the EAC Extension. Concurrent with this change in the eddy field are changes to the upper ocean stratification off southeast Australia with significant upper-ocean warming increasing the energy input to the thermocline. A stability analysis of the background ocean fields shows an increase in baroclinic and barotropic instability focused around the EAC separation point indicating a greater rate of energy being transferred into both the generation of mesoscale eddies (baroclinic instability) and the longevity of eddies (barotropic instability) [e.g., *Charney*, 1947; *Eady*, 1949; *Phillips*, 1954; *Gill et al*., 1974]. This was also supported by the growth period of eddy amplitudes in the region extending from the first 5 weeks in the CTRL to the first 10 weeks in the A1B run.

This study represents the first comprehensive analysis of identified and tracked mesoscale eddies in the Tasman Sea region based on future climate change projections. Previous studies have examined trends in eddy-related transport in the Tasman Sea [*van Sebille et al*., 2012; *Cetina-Heredia et al*., 2014]. Numerous studies have examined changes in circulation statistics associated with eddies (e.g., eddy kinetic energy) under climate change scenarios (e.g., *Farneti and Delworth* [2010], *Farneti et al*. [2010], and *Spence et al*. [2010] in the Southern Ocean; *Matear et al*. [2013] and *Oliver and Holbrook* [2014] in the Tasman Sea), but these did not identify and track individual eddies. Eddy identification and tracking has traditionally been difficult due to the coarse resolution of the ocean model component of coupled climate models (i.e., not eddy resolving, or eddy permitting at best). However, as eddy-resolving ocean models become more common in coupled climate models, this type of analysis is likely to be beneficial to quantifying and understanding the poleward transport contribution from eddies.

Two limitations of the present study should be noted here. First, the analysis of climate change projections is typically performed using an ensemble of models each run for a number of different emissions scenarios. The former allows for a reduction of model error by examining the multimodel ensemble mean and the latter takes account of multiple future scenarios. In the present study, the model simulations only consist of a single ocean model (OFAM) and a single carbon emissions scenario (A1B). The use of a single model implies that we cannot be certain of the uncertainties in the model projections. Nevertheless, we are confident in the modeling tools themselves, since model evaluation demonstrates that they are able to capture the historical record rather well [*Sun et al*., 2012; *Matear et al*., 2013; *Oliver and Holbrook*, 2014] (see *O'Kane et al*. [2011] for a more general discussion of the performance of OFAM). The use of a single carbon emissions scenario means that we provide projected transport estimates for a specific climate change case study, but since the real-world carbon emissions have already exceeded the trends prescribed for the A1B scenario, we can interpret the present study as providing conservative estimates of change. Second, the model simulations analyzed here do not integrate the ocean variability continuously over the 1990s to the 2060s period and, therefore, do not allow for internal variability in the coupled climate system but rather provide output for those individual decades under equilibrium conditions. Therefore, it is important to recognize that the results presented here represent only the equilibrium climate response to changes in carbon emissions.

Our findings link the projected changes in mean transport in the EAC Extension to concurrent changes in the mesoscale eddy field, both driven by anthropogenic climate change. The historical record indicates a clear spin-up of the South Pacific subtropical gyre [*Roemmich et al*., 2007] with an associated multidecadal trend in upper ocean warming in the Tasman Sea [*Holbrook and Bindoff*, 1997; *Ridgway*, 2007; *Wu et al*., 2012] and transport increase in the EAC and EAC Extension [*Cetina-Heredia et al*., 2014]. Recent studies of projected future climate change suggest an increase in transport across the EAC separation point and in the EAC Extension [*Sun et al*., 2012; *Matear et al*., 2013; *Oliver and Holbrook*, 2014; *Sloyan and O'Kane*, 2015], a hot spot of warming in the central Tasman Sea [*Matear et al*., 2013; *Oliver and Holbrook*, 2014], and an increase in sea surface temperature extreme events in the western Tasman Sea [*Oliver et al*., 2014]. Here based on our dynamical analysis of model output in the present study, we have shown that there is also

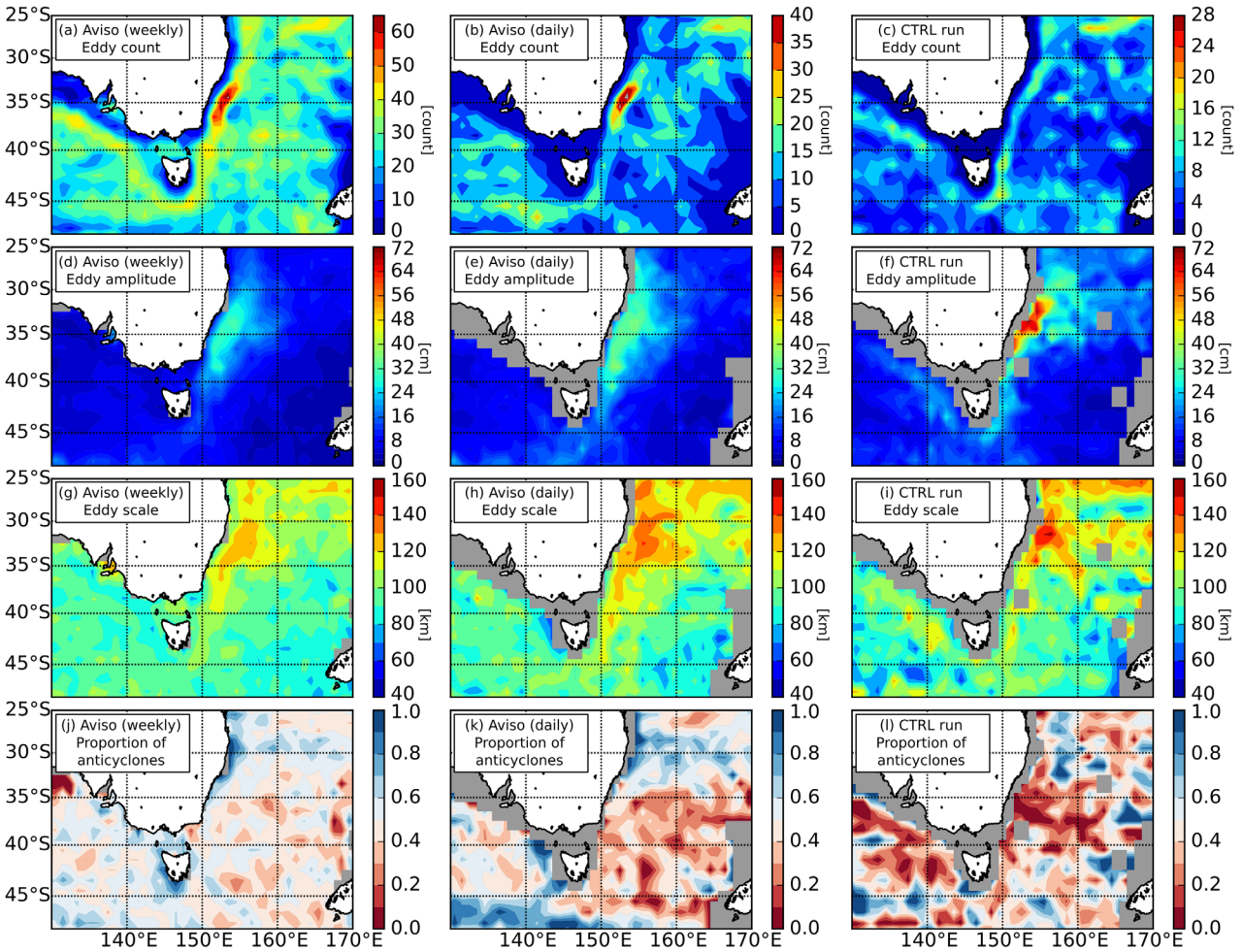

Figure 9. Comparison of tracked eddy summary statistics between observations and model. (first row) Total eddy count, (second row) average eddy amplitude, (third row) average eddy scale, and (fourth row) proportion of anticyclonic eddies are shown for (left column) the weekly Aviso data, (middle column) the daily Aviso data, and (right column) the OFAM CTRL run in the 1° gridded domain. A proportion of anticyclonic eddies equal to 1 indicates 100% anticyclonic eddies in that cell, 0 indicates no anticyclonic eddies (100% cyclonic eddies), and 0.5 indicates a 50%-50% split between anticyclonic and cyclonic eddies. Grey indicates areas of no data.

projected to be an increase in the number and stability of anticyclonic (warm-core) eddies in the EAC Extension.

The ability of mesoscale eddies to transport biophysical properties (temperature, salinity, nutrients, marine larvae) [e.g., *Everett et al.*, 2012] mean that projected changes in the eddy field can have significant impacts on the fragile cool-water marine ecosystems off southeastern Australia, particularly Tasmania, which have already undergone significant climate-related changes in recent decades [*Last et al.*, 2010; *Johnson et al.*, 2011; *Sunday et al.*, 2015]. These impacts could be event like in nature as nutrient-poor, low productivity, warm-core eddies propagate along the EAC extension and interact with the continental shelf. Large anticyclonic EAC eddies sitting east of Tasmania have been observed to wash warm water onto the continental shelf and cause sudden warm events along the coast, a region of high importance for aquaculture and marine biodiversity. An increase of larger eddies with warmer water trapped inside them could lead to larger and more frequent sudden warming events across the continental shelf, that may have dire consequences for local aquaculture (e.g., abalone, Atlantic salmon) and biodiversity (several species of temperature-sensitive kelp). In addition, mesoscale eddies are known to transport oceanic chlorophyll [*Chelton et al.*, 2011b] and can also retain pelagic fish larvae in relatively productive or unproductive habitats [*Asch and Checkley*, 2013]. An increase in the proportion of poor productivity anticyclonic eddies off southeastern Australia may reduce the productivity of pelagic fisheries, such as yellowfin tuna and albacore tuna

[e.g., *Hobday and Hartog*, 2014; *Dell et al*., 2015]. Alternatively, an increase in anticyclonic eddies could provide more feeding grounds for yellowfin tuna, which tend to aggregate along the edges of such eddies [*Young et al*., 2001].

Appendix A: Eddy Tracking Algorithm

We used the *Chelton et al*. [2011a] algorithm to detect and track mesoscale eddies in the CTRL and A1B OFAM ocean model simulations (Appendix B in that paper). This algorithm performs the eddy detection and tracking from fields of sea surface height (η). Briefly, eddies are first detected as contiguous regions of space for which (i) η is above a specified threshold, (ii) the area enclosed by each region is greater than the area of a circle with radius 0.4° (in latitude-longitude space), (iii) there is a local minimum or maximum of η for cyclonic or anticyclonic eddies, respectively, (iv) the peak amplitude is at least 1 cm, and (v) the linear dimension of the region is less than 400 km (only valid poleward of 25° latitude). Eddy detection was performed independently for each daily map of η. Eddy trajectories (tracks) were then generated for each eddy by searching for all eddy centroids at successive time steps that lie within a specified ellipsoid centered on the eddy. The dimensions of the ellipsoid are 150 km in the North-South direction and a length defined by the first baroclinic Rossby wave phase speed [*Chelton et al*., 1998] in the East-West direction. Further details of the algorithm can be found in *Chelton et al*. [2011a]; all thresholds defined by *Chelton et al*. [2011a] in pixels or time steps were scaled according to the ratio of grid spacings and time steps between Archiving, Validation, and Interpretation of Satellite Oceanographic Data (Aviso) and OFAM (1/4° versus 1/10° and 7 days versus 1 day, respectively).

In order to validate the eddy field from the CTRL simulation, we have calculated a suite of summary statistics from the detected and tracked eddies for the CTRL simulation as well as from observed sea levels. The observational data sets include the merged reference Aviso data (weekly 1/4° resolution fields, covering 16.8 years) and the recently released two-satellite data (daily 1/4° resolution fields, covering 21.8 years). This allows for a comparison of daily observations against weekly observations; unfortunately, there was no higher-resolution observed data set to allow a comparison at the same resolution as the ocean model (i.e., 1/10°). For all data sets, eddy statistics were evaluated within $1^\circ \times 1^\circ$ bins and include (i) the total number of eddies per bin, (ii) the average eddy amplitude in each bin, (iii) the average eddy scale in each bin, and (iv) the proportion of cyclonic and anticyclonic eddies in each bin.

Eddy statistics were generally similar across the two observed data sets and the CTRL simulation (Figure 9). Eddy counts peaked around the EAC separation region and were generally higher along a band running parallel to the east coast of Australia, i.e., along the EAC and EAC Extension pathway. This was evident in both observations and model simulations, and has been documented previously by *Everett et al*. [2012]. Eddy amplitudes were largest around the EAC separation point and along the EAC Extension. The model simulation overestimated the peak eddy amplitude in the EAC separation zone but predicted similar values along the EAC Extension as from the daily observations. Eddy scales also had the same pattern across the three data sets with peak values at, and north of, the EAC separation point and with a tongue of relatively larger eddy scales extending down the EAC Extension. The proportion of cyclonic to anticyclonic eddies was consistent across the three data sets. Eddies in the Tasman Sea and EAC Extension were predominantly anticyclonic while eddies to the north of the Tasman Front were predominantly cyclonic. We conclude that the eddies detected from the CTRL simulation have similar properties to those detected from Aviso sea level data.

Acknowledgments

E.C.J.O. and N.J.H. would like to acknowledge funding from the Australian Research Council (ARC) Super Science Fellowship (grant FS110200029) and the ARC Centre of Excellence for Climate System Science (grant CE110001028); T.J.O. would like to acknowledge funding for his ARC Future Fellowship (grant FT120100008). The authors would like to acknowledge Richard Matear and Matthew Chamberlain of CSIRO Marine and Atmospheric Research (Hobart, Australia) for helpful discussions and for providing the OFAM model output; the authors would also like to acknowledge Andrew Kiss of the University of New South Wales, Australian Defence Force Academy for helpful discussions. Finally, the authors would like to acknowledge the valuable comments from two anonymous reviewers, who helped to substantially improve the manuscript. The OFAM downscaling model was supported by the Western Australian Marine Science Institution (WAMSI) I Node 2 "Climate processes, predictability and impacts in a warming Indian Ocean". This paper makes a contribution to the objectives of the ARC Centre of Excellence for Climate System Science and the CLIVAR-endorsed Southwest Pacific Ocean Circulation and Climate Experiment (SPICE). E.C.J.O. would also like to acknowledge the ARCCSS 2014 Scientific Paper Writing Workshop by Peter Rothlisberg (CSIRO), including discussions with Byju Pakkandy (Monash University) and Ailie Gallant (Monash University), which helped to improve and finish this paper. All data used in the development of the manuscript were generated from the model data described by *Chamberlain et al*. [2012]; computer code for eddy detection, tracking, and calculating eddy properties is publicly available online (https://github.com/ecjoliver/eddyTracking).

References

Asch, R. G., and D. M. Checkley (2013), Dynamic height: A key variable for identifying the spawning habitat of small pelagic fishes, *Deep Sea Res., Part I*, *71*, 79–91.

Boland, F. M., and J. A. Church (1981), The East Australian Current 1978, *Deep Sea Res., Part A*, *28*(9), 937–957.

Böning, C. W., and R. G. Budich (1992), Eddy dynamics in a primitive equation model: Sensitivity to horizontal resolution and friction, *J. Phys. Oceanogr.*, *22*, 361–381.

Cetina-Heredia, P., M. Roughan, E. van Sebille, and M. A. Coleman (2014), Long-term trends in the East Australian Current separation latitude and eddy driven transport, *J. Geophys. Res. Oceans*, *119*, 4351–4366, doi:10.1002/2014JC010071.

Chamberlain, M. A., C. Sun, R. J. Matear, M. Feng, and S. J. Phipps (2012), Downscaling the climate change for oceans around Australia, *Geosci. Model Dev. Discuss.*, *5*, 425–458.
Charney, J. G. (1947), The dynamics of long waves in a baroclinic westerly current, *J. Meteorol.*, *4*(5), 136–162.
Chelton, D. B., R. A. Deszoeke, M. G. Schlax, K. El Naggar, and N. Siwertz (1998), Geographical variability of the first baroclinic Rossby radius of deformation, *J. Phys. Oceanogr.*, *28*(3), 433–460.
Chelton, D. B., M. G. Schlax, and R. M. Samelson (2011a), Global observations of nonlinear mesoscale eddies, *Prog. Oceanogr.*, *91*(2), 167–216.
Chelton, D. B., P. Gaube, M. G. Schlax, J. J. Early, and R. M. Samelson (2011b), The influence of nonlinear mesoscale eddies on near-surface oceanic chlorophyll, *Science*, *334*(6054), 328–332.
Dell, J. T., C. Wilcox, R. J. Matear, M. A. Chamberlain, and A. J. Hobday (2015), Potential impacts of climate change on the distribution of longline catches of yellowfin tuna (Thunnus albacares) in the Tasman sea, *Deep Sea Res., Part II*, *113*, 235–245.
Eady, E. T. (1949), Long waves and cyclone waves, *Tellus*, *1*(3), 33–52.
Early, J. J., R. M. Samelson, and D. B. Chelton (2011), The evolution and propagation of quasigeostrophic ocean eddies, *J. Phys. Oceanogr.*, *41*(8), 1535–1555.
Eden, C., and C. Böning (2002), Sources of eddy kinetic energy in the Labrador Sea, *J. Phys. Oceanogr.*, *32*(12), 3346–3363.
Everett, J. D., M. E. Baird, P. R. Oke, and I. M. Suthers (2012), An avenue of eddies: Quantifying the biophysical properties of mesoscale eddies in the Tasman Sea, *Geophys. Res. Lett.*, *39*, L16608, doi:10.1029/2012GL053091.
Farneti, R., and T. L. Delworth (2010), The role of mesoscale eddies in the remote oceanic response to altered Southern Hemisphere winds, *J. Phys. Oceanogr.*, *40*(10), 2348–2354.
Farneti, R., T. L. Delworth, A. J. Rosati, S. M. Griffies, and F. Zeng (2010), The role of mesoscale eddies in the rectification of the Southern Ocean response to climate change, *J. Phys. Oceanogr.*, *40*(7), 1539–1557.
Frusher, S. D., A. J. Hobday, S. M. Jennings, C. Creighton, D. D'Silva, M. Haward, N. J. Holbrook, M. Nursey-Bray, G. T. Pecl, and E. I. van Putten (2014), The short history of research in a marine climate change hotspot: From anecdote to adaptation in south-east Australia, *Rev. Fish Biol. Fish.*, *24*(2), 593–611.
Gill, A. E., J. S. A. Green, and A. J. Simmons (1974), Energy partition in the large-scale ocean circulation and the production of mid-ocean eddies, *Deep Sea Res. Oceanogr. Abstr.*, *21*, 499–528.
Godfrey, J. S., G. R. Cresswell, T. J. Golding, A. F. Pearce, and R. Boyd (1980), The separation of the East Australian Current, *J. Phys. Oceanogr.*, *10*(3), 430–440.
Hamon, B. (1965), The East Australian Current, 1960–1964, *Deep Sea Res. Oceanogr. Abstr.*, *12*(6), 899–921.
Hill, K., S. R. Rintoul, R. Coleman, and K. R. Ridgway (2008), Wind-forced low frequency variability of the East Australian Current, *Geophys. Res. Lett.*, *35*, L08602, doi:10.1029/2007GL032912.
Hobday, A. J., and J. R. Hartog (2014), Derived ocean features for dynamic ocean management, *Oceanography*, *27*(4), 134–145.
Holbrook, N. J., and N. L. Bindoff (1997), Interannual and decadal temperature variability in the southwest Pacific Ocean between 1955 and 1988, *J. Clim.*, *10*(5), 1035–1049.
IOC, SCOR, and IAPSO (2010), The international thermodynamic equation of seawater—2010: Calculation and use of thermodynamic properties, in *Intergovernmental Oceanographic Commission, Manuals and Guides No 56*, 196 pp., UNESCO (English).
Johnson, C. R., et al. (2011), Climate change cascades: Shifts in oceanography, species' ranges and subtidal marine community dynamics in eastern Tasmania, *J. Exp. Mar. Biol. Ecol.*, *400*(1), 17–32.
Joyce, T. M., S. L. Patterson, and R. C. Millard (1981), Anatomy of a cyclonic ring in the Drake Passage, *Deep Sea Res., Part A*, *28*(11), 1265–1287.
Last, P. R., W. T. White, D. C. Gledhill, A. J. Hobday, R. Brown, G. J. Edgar, and G. Pecl (2010), Long-term shifts in abundance and distribution of a temperate fish fauna: A response to climate change and fishing practices, *Global Ecol. Biogeogr.*, *20*, 58–72.
Mata, M. M., S. E. Wijffels, J. A. Church, and M. Tomczak (2006), Eddy shedding and energy conversions in the East Australian Current, *J. Geophys. Res.*, *111*, C09034, doi:10.1029/2006JC003592.
Matear, R. J., M. A. Chamberlain, C. Sun, and M. Feng (2013), Climate change projection of the Tasman Sea from an eddy-resolving ocean model, *J. Gephys. Res. Oceans*, *118*, 2961–2976, doi:10.1002/jgrc.20202.
Morrow, R., F. Fang, M. Fieux, and R. Molcard (2003), Anatomy of three warm-core Leeuwin Current eddies, *Deep Sea Res., Part II*, *50*(12), 2229–2243.
Nilsson, C. S., and G. R. Cresswell (1980), The formation and evolution of East Australian Current warm-core eddies, *Prog. Oceanogr.*, *9*(3), 133–183.
O'Kane, T. J., P. R. Oke, and P. A. Sandery (2011), Predicting the East Australian Current, *Ocean Modell.*, *38*(3), 251–266.
Oke, P. R., G. B. Brassington, D. A. Griffin, and A. Schiller (2008), The Bluelink ocean data assimilation system (BODAS), *Ocean Modell.*, *21*(1-2), 46–70.
Oliver, E. C. J., and N. J. Holbrook (2014), Extending our understanding of South Pacific gyre "spin-up": Modeling the East Australian Current in a future climate, *J. Geophys. Res. Oceans*, *119*, 2788–2805, doi:10.1002/2013JC009591.
Oliver, E. C. J., S. J. Wotherspoon, and N. J. Holbrook (2014), Projected Tasman Sea extremes in sea surface temperature through the 21st Century, *J. Clim.*, *27*(5), 1980–1998.
Peixoto, J. P., and A. H. Oort (1992), *Physics of Climate*, Am. Inst. of Phys., N. Y.
Phillips, N. A. (1954), Energy transformations and meridional circulations associated with simple baroclinic waves in a two-level, quasi-geostrophic model1, *Tellus*, *6*(3), 273–286.
Ridgway, K. R. (2007), Long-term trend and decadal variability of the southward penetration of the East Australian Current, *Geophys. Res. Lett.*, *34*, L13613, doi:10.1029/2007GL030393.
Ridgway, K. R., and J. R. Dunn (2003), Mesoscale structure of the mean East Australian Current System and its relationship with topography, *Prog. Oceanogr.*, *56*(2), 189–222.
Roemmich, D., J. Gilson, R. Davis, P. Sutton, S. Wijffels, and S. Riser (2007), Decadal spinup of the South Pacific subtropical gyre, *J. Phys. Oceanogr.*, *37*, 162–173.
Sloyan, B. M., and T. J. O'Kane (2015), Drivers of decadal variability in the Tasman Sea, *J. Geophys. Res. Oceans*, *120*, 3193–3210.
Spence, P., J. C. Fyfe, A. Montenegro, and A. J. Weaver (2010), Southern Ocean response to strengthening winds in an eddy-permitting global climate model, *J. Clim.*, *23*(19), 5332–5343.
Sun, C., M. Feng, R. J. Matear, M. A. Chamberlain, P. Craig, K. R. Ridgway, and A. Schiller (2012), Marine downscaling of a future climate scenario for Australian boundary currents, *J. Clim.*, *25*(8), 2947–2962.
Sunday, J. M., et al. (2015), Species traits and climate velocity explain geographic range shifts in an ocean-warming hotspot, *Ecol. Lett.*, *18*, 944–953.

Suthers, I. M., et al. (2011), The strengthening East Australian Current, its eddies and biological effects—An introduction and overview, *Deep Sea Res., Part II*, *58*(5), 538–546.
Talley, L. D. (2003), Shallow, intermediate, and deep overturning components of the global heat budget, *J. Phys. Oceanogr.*, *33*(3), 530–560.
Uppala, S. M., et al. (2005), The ERA-40 re-analysis, *Q. J. R. Meteorol. Soc.*, *131*(612), 2961–3012.
van Sebille, E., M. H. England, J. D. Zika, and B. M. Sloyan (2012), Tasman leakage in a fine-resolution ocean model, *Geophys. Res. Lett.*, *39*, L06601, doi:10.1029/2012GL051004.
Wu, L., et al. (2012), Enhanced warming over the global subtropical western boundary currents, *Nat. Clim. Change*, *2*(3), 161–166.
Young, J. W., R. Bradford, T. D. Lamb, L. A. Clementson, R. Kloser, and H. Galea (2001), Yellowfin tuna (Thunnus albacares) aggregations along the shelf break off south-eastern Australia: Links between inshore and offshore processes, *Mar. Freshwater Res.*, *52*(4), 463–474.